IDENTIFICATION AND ELECTROMAGNETIC CONTROL OF STRUCTURES IN RAYLEIGH-BÉNARD CONVECTION

Jos Verdoold, Peter Witte, Lambertus Hoek, Mark J. Tummers, Kemo Hanjalić
Department of Multi-Scale Physics,
Delft University of Technology
P.O. Box 5046, 2600 GA Delft, The Netherlands
j.verdoold@ws.tn.tudelft.nl

ABSTRACT

The paper reports on an investigation of turbulent flow structures in a large aspect-ratio (W:H=4:1) Rayleigh-Bénard convection cell and their correlation with the instantaneous heat transfer. The final aim of the work is to manipulate these structures by means of electromagnetic (EM) forces that are concentrated in a thin region adjacent to the bottom wall, thus enabling to exert a body force on the fluid in the boundary layer (Verdoold et al., 2003). While many issues are still to be addressed, this abstract reports on some interesting results obtained in absence of the EM forcing. In RB convection the formation of plumes and their impingement is associated with motion in the wall boundary layers, governing the heat transfer. We report on a quantitative investigation of distinct structures and spoke patterns in the temperature field in the vicinity of the boundary layer, which have been visualised earlier by e.g. Theerthan and Arakeri (2000) and others.

INTRODUCTION

The numerical study of coherent structures in classic and magnetic Rayleigh-Bénard (RB) convection, e.g. Hanjalić and Kenjereš (2000) revealed a striking reorganisation of the vortical structures when a homogeneous, vertical magnetic field is applied. This reorganisation was found to suppress significantly heat transfer in proportion (though not linearly) to the intensity of the imposed magnetic field. Moreover, a specific magnetic field of a limited spatial extent, stretching only over the thin near-wall region (what can easily be achieved in an experiment or application with discrete permanent magnets attached to a wall) can produce desired restructuring of the wall layers and damp or enhance heat transfer according to needs (Kenjereš and Hanjalić, 2004; Verdoold et al., 2003). The ongoing research, which is partly reported here has been aimed at investigating coherent structure in a flow in a box driven separately by thermal buoyancy or by an electromagnetic force, as well as by their simultaneous action, with an ultimate aim of achieving desirable control of flow and heat transfer. In the present paper we report on pure buoyancy driven flows, i.e. in a classic setup for RB convection of a sufficiently large aspect ratio to mimic a true infinite thermal convection with negligible side-wall effects.

Rayleigh-Bénard convection has served long as a convenient generic configuration for studying pure thermal convection. When a fluid is confined between two constant temperature walls, where the bottom one has a higher temperature than the upper wall, diffusive heat transfer from the bottom wall will locally create lighter fluid densities (at the bottom wall). These perturbations lead to horizontal density perturbations. Pressure variations in their turn move the less dense fluid into a boundary layer near the bottom wall. When this boundary layer extends itself horizontally, it will become unstable at a certain thickness because of gravitational instability. This instability generates the eruption of warm fluid from the boundary layer in the form of thermal plumes. From their generation near the bottom wall, the small plumes tend to group and lead to distinct patterns. Zocchi et al. (1990) and Theerthan and Arakeri (2000) investigated these patterns experimentally in a qualitative way. Kerr and Herring (2000), for example, did this numerically for $Ra \sim 10^7$, $Pr = 7.0$ with a direct numerical simulation.

While many phenomena are still to be addressed, we present here some results on instantaneous temperature and velocity measurements as well as the combination of both. The paper will focus on long-term velocity measurements with laser Doppler anemometry (LDA) in different parts of a convection cell. Furthermore, detailed planar measurements of temperature, using liquid crystal thermography (LCT), and velocity, using particle image velocimetry (PIV), in the boundary layer and near the wall will be presented. The final goal will be to apply the knowledge gained from this paper in combination with Verdoold et al. (2003), to actively impose a scaling upon a thermal convective flow.

EXPERIMENTAL METHOD

The Rayleigh-Bénard set-up consists of a $600 \times 600 \times 155$ mm^3 ($W \times W \times H$) tank which is depicted in Figure 1. Water is used as a working fluid, but for the electromagnetic experiments a Na_2SO_4 electrolyte solution will be used instead to provide a larger conductivity. Two copper plates at the top and at the bottom are kept at a constant temperature by pumping water through them from two basins containing constant temperature water. By doing so, the plates impose a controlled temperature gradient on the working fluid. Experiments were conducted at a Rayleigh number $Ra = 1.3 \times 10^8$, corresponding to a temperature difference of 3.8°C. The mean temperature of the working fluid was approximately 20°C giving a Prandtl number of 7.0.

The origin of a Cartesian coordinate system was chosen to coincide with the centre of the bottom wall, see Fig. 1. The x and y-coordinates are measured along the lower wall, parallel to the side walls of the RB cell. The z-coordinate measures the wall normal distance.

Laser Doppler Anemometry

The LDA measurements were performed using a two-component, dual beam system manufactured by Dantec. The green (514.5 nm) and blue (488.0 nm) colours of a 5 W Argon-ion laser were used to measure two velocity components simultaneously. One beam of each colour was frequency pre-shifted by a Bragg cell to enable the detection of instantaneous flow reversals. The two beam pairs were oriented such that the wall normal and a wall parallel velocity component were measured directly. A small tilt angle was introduced to allow for measurements close to the wall. The length and diameter of the two overlapping measurement volumes are 0.8 mm and 0.1 mm, respectively, which is sufficiently small to resolve the smallest length scales of the flow.

The light scattered by 5 μm polyamid seed particles (Dantec) was collected in forward direction, then split into its components and subsequently focused on two photomultipliers. The photomultiplier output signals were electronically downmixed, and then fed to two Dantec BSA signal processors. The LDA system measured the instantaneous velocities of the seed particles with an inaccuracy of 0.5% as will be shown later.

LDA measurements were taken in twenty points distributed along a wall normal in the centre of the RB cell at $x = 0$, $y = 0$. At each point approximately 3×10^5 samples were collected at a mean rate of approximately 30 Hz. The resulting very long measuring times ($\approx 10^4$ s) are needed to obtain temporal convergence of the statistical quantities such as mean velocity and variance of the velocity fluctuations.

Particle Image Velocimetry

The velocity field was measured by using a PIV system that included a Continuum Minilite double-pulsed Nd:YAG laser with a pulse energy of 25 mJ. This laser produced an approximately 1 mm thick light sheet that illuminated the seeding particles in the flow. Hollow glass spheres (Potters-Ballotini) with a diameter of approximately 10 μm were used as seed particles. These particles were mixed with the working fluid in a concentration of approximately 1.0×10^{-2} g l^{-1}.

A PCO Sensicam camera with a resolution of 1280×1024 pixels recorded images of the seed particles in the light sheet. A 55 mm focal length lens with a numerical aperture $f^{\#} = 4$ was mounted on the PCO camera. Due to the small maximum velocity the time separation between pulses was set to 25 ms.

PIV measurements were performed near the x, z-midplane of the measurement volume at $y = -0.01$ m. The image pairs were analysed using the commercial software VidPIV Rowan v4.0 in three subsequent steps. The first step consists of cross-correlating non-overlapping interrogation areas of 32×32 pixels. Then, an adaptive cross-correlation with 50% overlapping interrogation areas of the same size is carried out. Finally, another adaptive cross-correlation is carried out for areas of 16×16 pixels, corresponding to areas in the measurement plane with size 0.16×0.16 cm^2. After each step spurious vector data are removed using a Gaussian interpolation local median filter with a kernel size of 3×3 surrounding interrogation zones. The number of non-valid vectors is about 2 percent of the total number of vectors.

Liquid Crystal Thermography

Temperature fields were obtained by using two variants of the Liquid Crystal Thermography (LCT) measurement technique. First, a thermochromic liquid crystal sheet with a measureable temperature range of 5 K (Hallcrest, R30C5WA) was mounted on the bottom plate of the RB cell. Since the top wall of the RB cell is not transparent, the colour camera (PCO Sensicam) viewed the liquid crystal sheet through one of the (glass) side walls. To obtain sharp, in-focus images a Schleimpflug tilt adapter was used to remove perspective blur. Using an in-situ hue-versus-temperature calibration and a dewarping technique, temperature fields on the bottom wall, i.e. the x, y-plane, could be determined accurately (± 0.05 K).

Secondly, temperature distributions in vertical x, z-planes were measured by using suspended liquid crystals (Hallcrest,

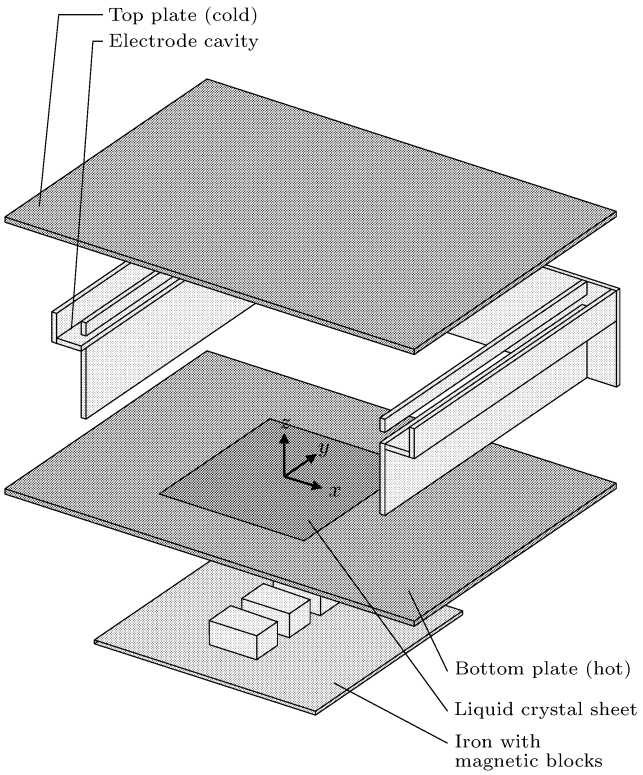

(a) Exploded view

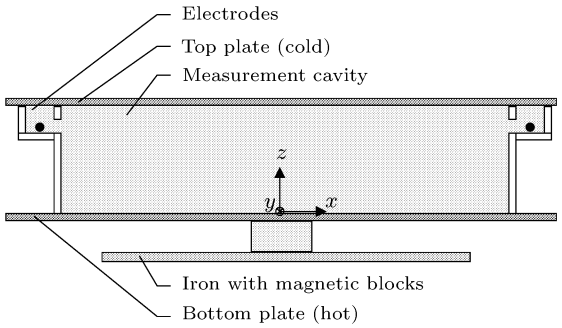

(b) Side view

Figure 1: Experimental set-up

R15C10W, 0.3 vol. %, temperature range 10 K). These micro-encapsulated liquid crystal particles are observed under an angle of 90 degrees, which reduces the effective temperature range to 2 K.

For both liquid crystal techniques the RGB data from the colour camera is converted to the Hue component (H) of the Hue, Saturation, Value (HSV) colour space by using $H = \arctan \sqrt{3}(G-B)/(2R-G-B)$ (Hay and Hollingsworth, 1996). A bijective relation between Hue and temperature can be found by performing an in-situ calibration that takes into account variations in experimental conditions like e.g. the lighting system, viewing and refraction angles.

RESULTS AND DISCUSSION

Results of the LDA measurements

Figure 2(a) shows a 200 s segment of a time series for the wall-parallel velocity component u, measured at 60 mm from the bottom wall. The total length of the time series is 1.2×10^4 s, and the samples were collected at a mean rate of 46 Hz. The long time series was used to determine the autocorrelation function (acf) of the velocity component u. Since the LDA system samples the velocity at random instants in time a special algorithm, known as the locally-scaled slotted correlation method (Tummers and Passchier, 1996) was used to compute the acf. A detailed view of the acf for short lag times is given in Fig. 3. Small errors in the instantaneous velocity cause a small discontinuity in the measured acf so that its value at zero lag time is 0.9946 instead of 1. The size of this discontinuity is a direct measure for the magnitude of the errors in the instantaneous velocity: $\sigma = (\overline{u'^2}(1 - 0.9946))^{1/2} = 3.2 \times 10^{-4}$ m/s, where σ is the width of a distribution. If it is assumed that the errors have a Gaussian distribution, then 97 % of all errors are within a $\pm 2\sigma$-band. This perfectly matches the width of the narrow noise band that can be observed in Fig. 2(a) for those moments when the instantaneous velocity remains nearly constant.

The measured acf shown in Fig. 3 is very smooth near zero lag time due to the low noise levels in the instantaneous velocity, and the use of the locally scaled version of the slotted correlation method. It appeared to be possible to accurately fit a parabola, $a_0 - (\tau/\lambda)^2$, to the measured correlation coefficients yielding a Taylor micro time scale of $\lambda = 2.8$ s. It is also seen that there is negligible change in the acf between $\tau = 0$ and $\tau = 1/46 \approx 0.022$ s, indicating that the mean data rate of 46 Hz is sufficiently high to resolve the smallest time scales of the flow.

The longer segment of the velocity time series shown in Fig. 2(b) indicates the presence of a large scale, quasi-periodic motion. This was investigated further by measuring acfs at other wall distances as well. As can be seen from the acf in Fig. 4 (left), the period of the large scale motion is approximately 325 s, while the amplitude of the period is 0.2, indicating that 20% of the power in the velocity fluctuations is due to the low-frequency oscillation.

The acfs that were measured closer to the lower wall at 6.0 mm (Fig. 4, centre) and at 2.5 mm (Fig. 4, right) also indicated the presence of a periodic component. Interestingly, both the amplitude and the frequency of the periodic motion appears to increase with decreasing wall distance.

The existence of a periodic motion is a well known phenomenon in RB convection for $Ra > 1.5 \times 10^7$. It has been reported in literature that in RB cells with an aspect ratio of about 1, the periodicity is related to the formation of a single large scale circulation (see for example Qiu et al. (2004)). The interaction between this large scale circulation and thermal plume formation is a topic of intense research, and, to the knowledge of the authors, this is the first time that a similar periodicity has been reported in a RB cell with a larger aspect ratio ($W/H = 4$).

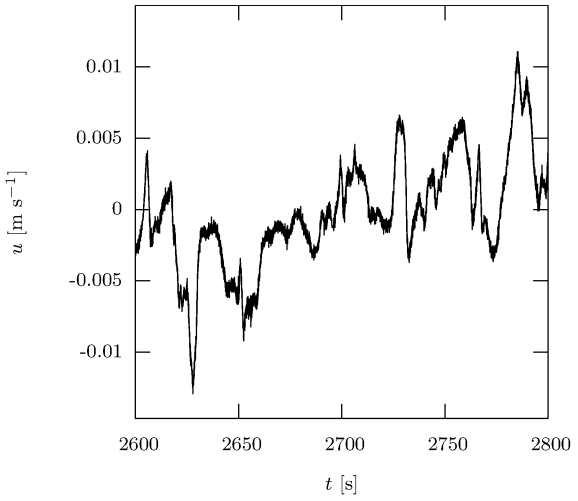

(a)

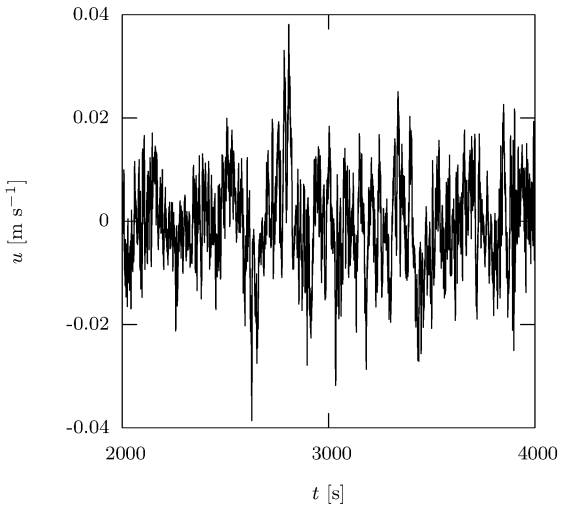

(b)

Figure 2: Short term (a) and long term (b) velocity measurements at $z = 73$ mm.

Results of the LCT and PIV measurements

Figure 5 depicts three sequential snapshots of simultaneously measured temperature and velocity fields. The time interval between the snapshots is 10 s. The temperature fields were obtained from the liquid crystal sheet mounted on the wall (x, y-plane), whereas the velocity field was measured in

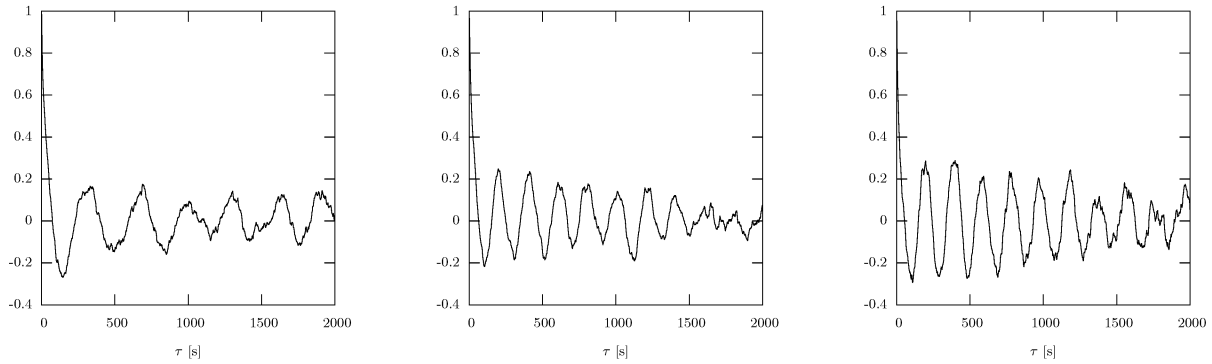

Figure 4: Autocorrelation functions of wall-parallel component u at $z = 60.0$ mm (left), $z = 6.0$ mm (centre) and $z = 2.5$ mm (right).

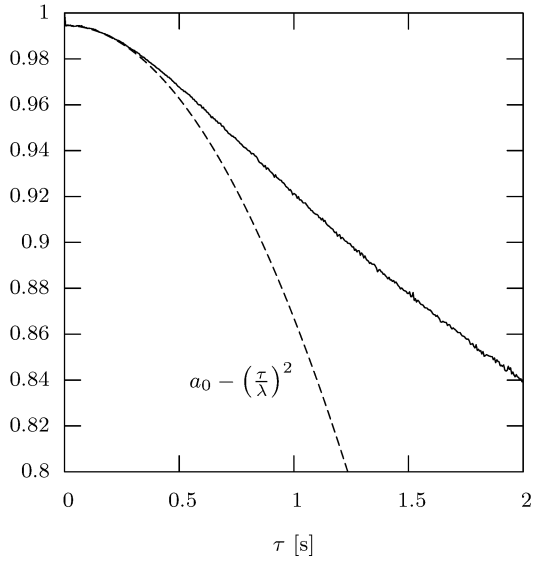

Figure 3: Autocorrelation function $\rho(\tau)$ and fitted parabola for obtaining Taylor micro-scale, $\lambda = 2800$ ms, $a_0 = 0.9946$

a vertical plane ($y = -10$ mm). The dashed line in the temperature fields marks the location of the PIV measurement plane.

It is clear from Fig. 5 that the hot regions are organised in narrow zones that enclose larger cold regions. These characteristic planform structures move slowly along the bottom wall with a velocity of about 2 mm/s, and have varying sizes with an upper limit of about 7 cm. The patterns observed in the present experiment (with $Ra = 1.3 \times 10^8$) are qualitatively similar to those observed by Theerthan and Arakeri (1994) for $Ra = 4.0 \times 10^7$ although the largest structures in their investigation were smaller ($\approx$ 3 cm). These differences may be caused by differences in the Rayleigh number, or by differences in the boundary conditions as the present experiment uses constant temperature plates, whereas Theerthan and Arakeri (1994) used poorly conducting surfaces.

Using the calibrated wall-mounted liquid crystal sheets we could quantify the temperature and temperature gradients in the boundary layer on the bottom wall. The gradient near the line plumes is quite steep, about 0.5 K, where the applied temperature difference ΔT between the cold and warm plates was 3.8 K. The temperature observed in these areas varies only little, (29.6±0.1)°C, which shows that downward moving fluid is descending in a more quiescent way.

The combined measurement of temperature and velocity gives more insight in the dynamics near the wall. Concentrating on the plume that is marked as A in Fig. 5 (left), it can be seen that the fluid is being accelerated above the hot region, and with increasing time it penetrates further into the descending (presumably) cold surroundings. Above the hot region marked as B we do not observe rising fluid. Instead, fluid appears to move in an almost horizontal direction towards the rising material above A, suggesting that the two sheets with hot fluid are connected.

Cold fluid can be seen impinging on the bottom wall near C. After impingement the fluid spreads away from the impingement point, and some of the fluid moves towards the rising plume. Generally speaking, the impingement process displaces the hot material in the thermal boundary layer radially away, and causes a local thinning of the thermal boundary layer thus promoting conductive heat transfer between the hot wall and the cold fluid. The hot fluid accumulates in narrow zones, and eventually erupts from the thermal boundary layer as a hot sheet which we recognise a thermal plume.

The latter part of this process is displayed quantitatively in Fig. 6 in a series of snapshots of temperature distributions in a vertical plane near the wall as determined with the suspended liquid crystals. The time interval between the images is 2 s. The first snapshots in Fig. 6 show an accumulation of heat within the boundary layer thus forming a bulge. Hot fluid erupts from the bulge, and rises vertically in a thin sheet. The thickness of this sheet appears to decrease when the plume continues to rise. While moving further upwards the plume decelerates and cools down due to heat transfer with the cold surroundings.

A typical mushroom-type structure appears since the orientation of the vertical plane is normal to the spanwise direction of the thermal plume. The vertical rise velocity of the plume indicates that at this particular moment the convection velocity of a possible large scale circulation is either zero or normal to the plane in which the temperature distribution is measured.

When the heat flux from the thermal boundary layer decreases, as can be seen in the temperature field in the last snapshots of Fig. 6, the centre part of the plume decays due to shear near the *trunk* of the plume and finally leaves both edges consisting of still relatively warm fluid as separately moving structures in the flow. Surprisingly these relative warm

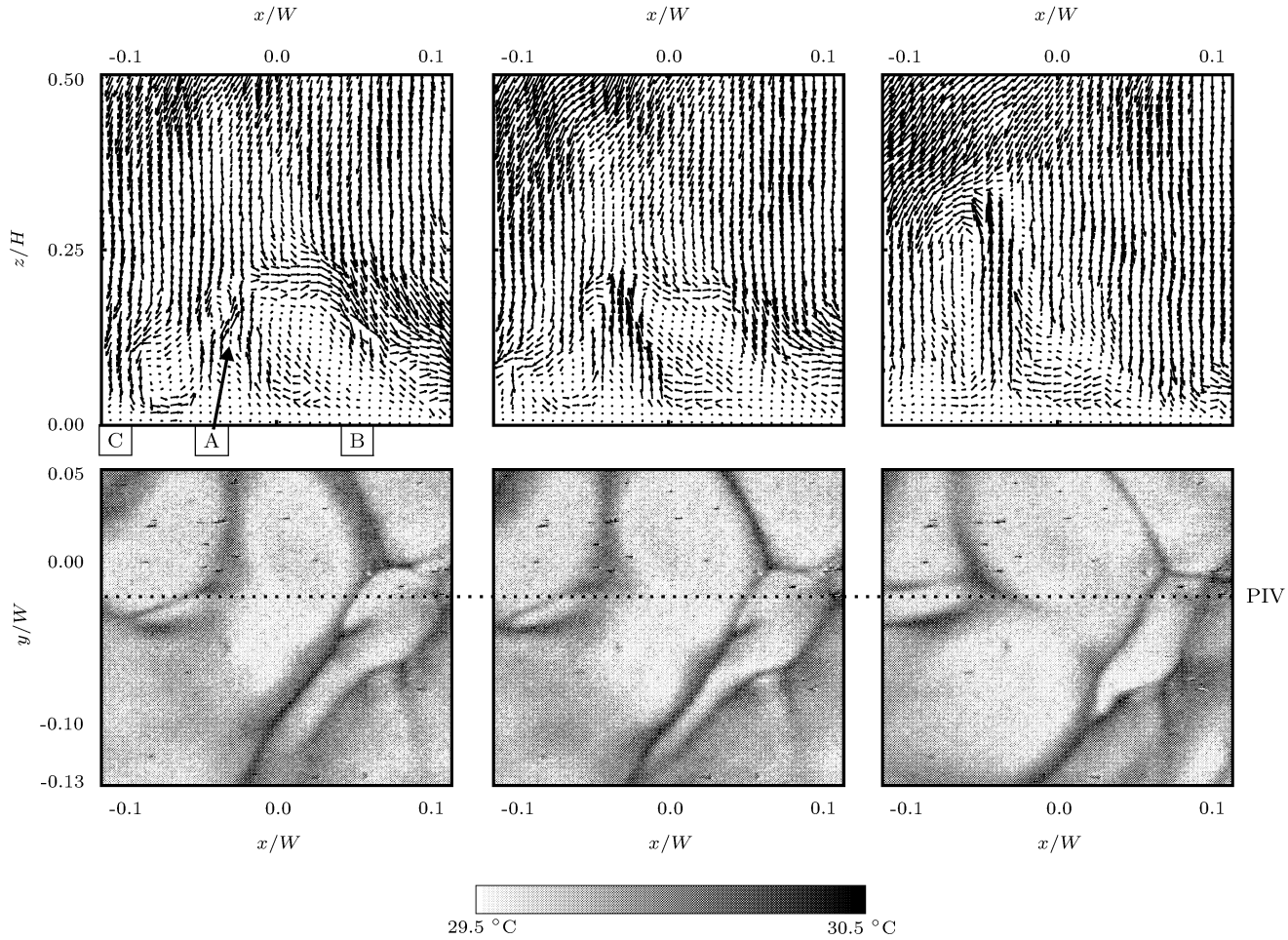

Figure 5: Three sequential snapshots of simultaneously measured velocity fields in the x, z-plane and temperature fields near the bottom wall (x, y-plane).

structures are advected downward due to the shear of the surrounding cold fluid, while one would expect they would tend to rise due to buoyancy. We observed that these structures which are separated from the boundary layer transport warm fluid quite efficient, being less vulnerable for mixing with downward moving fluid than the plumes.

CONCLUSIONS

Various optical measurement techniques, such as laser Doppler anemometry (LDA), liquid crystal thermography (LCT), and particle image velocimetry (PIV), were used to study structures in Rayleigh-Bénard convection The LDA experiments indicated the presence of a low-frequency oscillation with a much larger time scale than the time scales associated with the vortices. The combined measurement of temperature with LCT and velocity using PIV gives a better understanding of the dynamics near the wall by quantifying temperatures and extracting simultaneous velocity fields normal to it. The suspended LCT experiments gave insight on the vertical structure of thermal plumes as well as its creation and decay. For future experiments, the simultaneous use of suspended LCT and PIV would give us flow and temperature characteristics in the same plane and more details about the actual creation and decay of thermal plumes. The information on the scaling of the thermal structures will eventually give the input to actively control these thermal structures with electromagnetic forcing.

REFERENCES

Hanjalić, K. and Kenjereš, S., 2000, "Reorganization of Turbulence Structure in Magnetic Rayleigh-Bénard Convection: a T-RANS Study", *Journal of Turbulence*, Vol. 1, 22 pp.

Hay, J. L. and Hollingsworth, D. K., 1996, "A Comparison of Trichromic Systems for Use in the Calibration of Polymer-Dispersed Thermochromic Liquid Crystals", *Experimental Thermal and Fluid Science*, Vol. 12, pp. 1–12.

Kenjereš, S. and Hanjalić, K., 2004, "Numerical Simulation of Magnetic Control of Heat Transfer in Thermal Convection", *International Journal of Heat and Fluid Flow*, Vol. 25, pp. 559–568.

Kerr, R. M. and Herring, J. R., 2000, "Prandtl Number Dependence of Nusselt Number in Direct Numerical Simulations", *Journal of Fluid Mechanics*, Vol. 419, pp. 325–344.

Qiu, X., Shang, X., Tong, P., and Xia, K., 2004, "Velocity oscillations in turbulent Rayleigh-Benard convection", *Physics of Fluids*, Vol. 16, pp. 412–423.

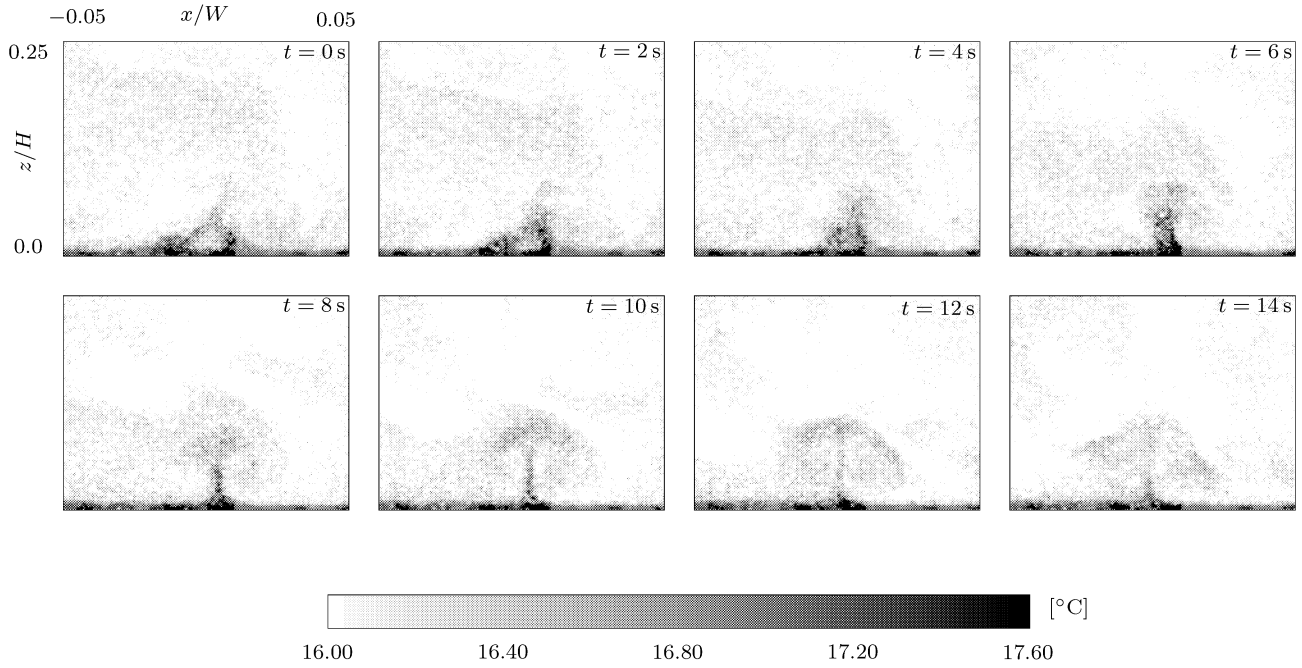

Figure 6: Sequential snapshots of temperature distribution in the x, z-plane. The field of view is 40×60 mm^2.

Theerthan, S. A. and Arakeri, J. H., 1994, "Planform Structure of Turbulent Rayleigh-Bénard Convection", *International Communication in Heat and Mass Transfer*, Vol. 21, pp. 561–572.

Theerthan, S. A. and Arakeri, J. H., 2000, "Planform Structure and Heat Transfer in Turbulent Free Convection over Horizontal Surfaces", *Physics of Fluids*, Vol. 12, pp. 884–894.

Tummers, M. and Passchier, D., 1996, "Spectral estimation using a variable window and the slotting technique with local normalization", *Measurement Science & Technology*, Vol. 7, pp. 1541–1546.

Verdoold, J., Rossi, L., Tummers, M. J., and Hanjalić, K., 2003, "Towards Electromagnetic Control of Thermal Convection", *Proceedings of the 7th International Symposium on Fluid Control, Measurement and Visualization*.

Zocchi, G., Moses, E., and Libchaber, A., 1990, "Coherent Structures in Turbulent Convection, an Experimental Study", *Physica A*, Vol. 166, pp. 387–407.